Liquid-crystal Hartmann wave-front scanner

Ségolène Olivier, Vincent Laude, and Jean-Pierre Huignard

The liquid-crystal wave-front scanner (LCWS) is a highly sensitive wave-front sensor suited to the measurement of aberrations in optical systems and, more generally, of static wave fronts, and it is based on the Hartmann test. In the LCWS an incoming wave front is scanned sequentially by a programmable moving aperture that is implemented by use of a liquid-crystal display. The position of the diffraction spot is recorded behind an observation lens with a CCD detector and provides an estimation of the local slopes in two orthogonal directions at the aperture position. The wave front is then reconstructed from slope data by use of a least-squares method. Experiments are reported for nearly planar wave fronts as well as for strongly aberrated wave fronts, demonstrating both the large dynamic range and the great sensitivity of the LCWS. The LCWS is compared with the Shack–Hartmann wave-front sensor in terms of dynamic range and sensitivity. © 2000 Optical Society of America

OCIS codes: 010.7350, 120.5050, 230.6120.

1. Introduction

Wave-front sensors of different types are widely used in adaptive optics for astronomy,[1] the analysis of laser beams, and noncontact testing of optical components. These different applications have their particular characteristics and requirements, and no single wave-front sensor has clear advantages for all of them at once. In optical testing, only static aberrations have to be measured, but the required precision is generally more stringent than that for adaptive optics or laser-beam sensing. The different wave-front sensors can be divided into three groups, depending on whether they measure the phase directly or they estimate the wave front from the measurement of the first or the second derivative, i.e., the slope or the curvature, respectively, of the wave front. Phase-difference sensors, e.g., Michelson, Twymann–Green, and Fizeau interferometers,[1] provide a direct measurement of the wave-front phase at some wavelength compared with some reference wave-front phase. They are widely used for optical testing. The Shack–Hartmann sensor[2] and the three-wave lateral-shearing interferometer[3] are two examples of wave-front sensors that reconstruct the wave front from the measurement of the local slopes. Curvature-sensing devices[4] were recently introduced and are based on the ombroscopy technique.

The wave-front sensor[5] discussed in this paper belongs to the second group and is based on the Hartmann test, which provides a measurement of the local derivatives of the wave front in two orthogonal directions. In the original Hartmann test the light going through a small hole in an opaque mask that is superimposed on the incident wave front forms a diffraction-limited spot in the focal plane of an observation lens. The spot is shifted laterally, according to the local slope of the wave front at the aperture position. The Shack–Hartmann wave-front sensor (SHWS) provides a major improvement over the Hartmann test. It uses an array of lenslets to replace the single or the multiple holes in a mask. Each lenslet produces a diffraction-limited spot on a detector placed in the focal plane of the array. The local wave-front slopes are directly proportional to the displacement of the spots from the focal points of each lens. The number of lenslets determines the number of sampling points for the wave front and therefore its transverse resolution. The main advantage of this sensor is its real-time operation because all sampling points are obtained at once; however, it is not suited to the control of optical components that exhibit either very significant or very small wave-front variations. On the one hand, the maximal deviation of the spot behind each lenslet should not exceed the aperture of the microlens if a

reliable measurement is to be obtained without ambiguity. On the other hand, the focal length of the lenslet is generally short, say, a few centimeters, so the sensor is not sensitive to small variations of the slopes.

In the liquid-crystal Hartmann wave-front scanner introduced in Ref. 5 the mask of the Hartmann test was made programmable by use of a liquid-crystal television (LCTV): The wave front is scanned with a programmable aperture that moves sequentially across the analysis pupil of the wave front. The position of the diffraction spot in the focal plane of the observation lens is recorded for each sample. The wave front is then reconstructed from the slope data in a zonal or a modal way, just like in the Shack–Hartmann case. Compared with the SHWS, the Hartmann wave-front scanner is much more flexible because its dynamic range can be adapted to the object under measurement either by variation of the focal length of the observation lens or of the size and the shape of the sampling apertures in a nonuniform way. Moreover, as the whole surface of the detector is used for each sampling point, the liquid-crystal wave-front scanner (LCWS) benefits from a greater accuracy-to-dynamics ratio than does the SHWS. However, this increase is obtained by the sacrifice of real-time operation because the measurement of the wave front is sequential. Consequently, the field of use of the LCWS is the measurement of static wave fronts, which are required to be known with high accuracy.

The paper is organized as follows: In Section 2, we describe the principle of our wave-front sensor. An optical setup that uses a liquid-crystal (LC) display (LCD) as the programmable scanning aperture is presented in Section 3. In Section 4, we briefly outline the modal reconstruction algorithm used to estimate the wave front from the measurement of its local slopes. In Section 5, we report experimental results of reconstructed wave fronts obtained by transmission through various optical components and discuss the characteristics of the LCWS in terms of dynamics, sensitivity, and accuracy. Compared with a SHWS, the LCWS trades speed of operation for resolution, as is explained in Section 6. There are a number of other devices for sequential Hartmann wave-front sensors that were proposed prior to ours; differences between these solutions and ours are also discussed in Section 6. Section 7 concludes the paper.

2. Principle

The principle of operation of the LCWS is depicted in Fig. 1(a). Sampling of the wave front is accomplished by the sequential movement of a small aperture by use of a programmable pupil plane, which is implemented with a LCTV and the measurement for each sample of the displacement of the diffraction spot from its position when the incoming wave front is a plane wave. Calibration prior to the measurement of the optical component aims at eliminating the distortions of the wave front that are introduced by the optical setup itself or that are due to imper-
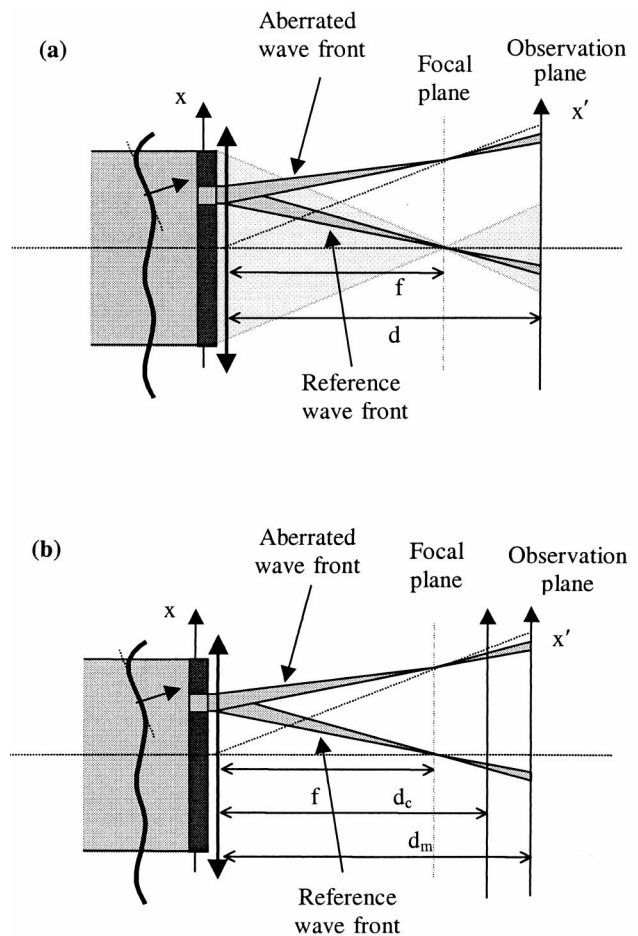

Fig. 1. Principle of the operation of the Hartmann wave-front scanner: (a) observation of the diffraction spots near the focal plane of the lens and (b) calibration and measurement of the optical system in two different planes.

fections of the illuminating laser beam. It is well known that the displacement of the diffraction spot in the focal plane of the lens is proportional to the average value of the wave-front slope inside the aperture at the pupil plane. For the reasons given below the diffraction spots are not necessarily observed in the focal plane but are observed somewhere close to the focal plane at a distance d from the lens. The average slope in the x direction of the wave front $W(x, y)$ is estimated from the displacement x' of the diffraction spot, as given by

$$\frac{\partial W(x, y)}{\partial x} = s(x, y) = \frac{x'}{d} - \left(\frac{1}{d} - \frac{1}{f}\right)x, \qquad (1)$$

where f is the focal length. A similar expression holds for the y direction. Equation (1) is for just one measurement. If a calibration x_c' is made at an observation distance d_c before the measurement x_m' is taken at distance d_m the estimated average slope reads as

$$s(x, y) = \frac{x_m'}{d_m} - \frac{x_c'}{d_c} - \left(\frac{1}{d_m} - \frac{1}{d_c}\right)x. \qquad (2)$$

Generally, calibration and measurement would be performed at the same distance d, in which case Eq. (2) simplifies to $\partial W(x, y)/\partial x = (x_m' - x_c')/d$ and is independent of the aperture position x. However, in certain cases the very different nature of the calibration and the measurement wave fronts can require different observation distances, as is depicted in Fig. 1(b); this might occur, for instance, if a strongly convergent or a strongly divergent sample were to be measured. In this configuration the measurement of the tilt aberration should be taken with caution because the spot positions are measured modulo a possible transverse translation that is caused by the camera motion.

It is apparent from Eq. (1) or Eq. (2) that the angular sensitivity of the LCWS is directly proportional to the observation distance d. Hence this observation distance should be maximized for the best accuracy. At the same time all diffraction spots must fall within the sensitive area of the CCD camera, which sets an upper limit on the observation distance that is dependent on the repartition of the wave-front slopes. The focal length f can thus be chosen on the basis of on the wave-front characteristics to accommodate the required dynamic range. This is a major difference from the SHWS in which the focal length is fixed by the lenslet array and remains short, say, a few centimeters.

The programmable pupil of the wave-front scanner consists of a LCTV that is electrically addressed and operates in transmission. Such a LCTV provides many precise and individually controllable apertures—the LCTV pixels—and can be driven electronically, for instance, by use of video signals. The LCTV pixels are smaller than the apertures required for wave-front sampling and can thus be grouped to yield rather arbitrary aperture shapes; this is again a major difference from the SHWS in which the sampling geometry is imposed by the lenslet array. The LCTV that we used is described in more detail in Section 3.

Let us note that a LC device placed between polarizers will in general produce amplitude and phase modulation. For the LCWS, binary amplitude modulation is preferable: One or several pixels of the LCTV are monitored to be transparent, whereas the rest of the pixels block the light; a constant phase over the aperture will not perturb the measurement. Another general characteristics of LCTV's explains why the detection plane should not be the focal plane. The binary amplitude modulation is not ideal, i.e., the contrast between the pixels that define the aperture and the other pixels is not infinite and has a typical value of 100. The diffraction pattern coming from the OFF part of the LCTV, which is much larger than the sampling aperture, can, however, be more powerful than the measurement spot. Moreover, for a plane wave front this pattern will come to a sharp focus near the focal plane. Because of the small size of the sampling aperture compared with the pupil size, the depth of focus of the measurement spot is much larger than that of the OFF diffraction pattern.
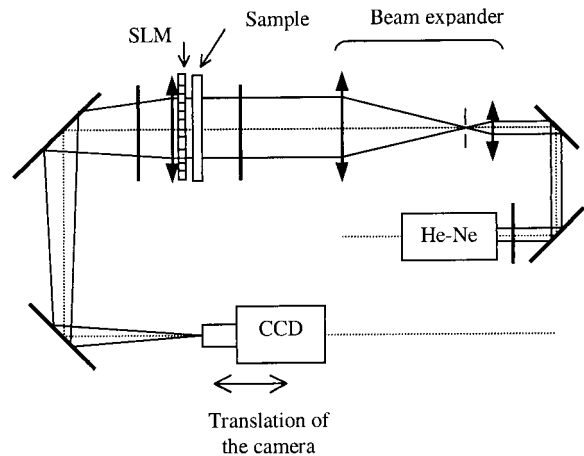

Fig. 2. Optical setup of the LCWS.

Displacement of the observation plane by some distance away from the focal plane thus offers a simple remedy to the contrast problem.

3. Optical Setup

We set up a laboratory demonstration of the LCWS on a breadboard (900 mm $\times$ 300 mm). The experimental setup is devoted to the testing of optical components in transmission, as is shown in Fig. 2. The incident light used to analyze the optical component in transmission is an expanded He–Ne laser beam ($\lambda = 632.8$ nm). The sample to be analyzed is placed just in front of the LCTV to analyze the wave front before it is affected by propagation or undergoes diffraction by the LCTV pixels. The LCTV used[6] is a commercial VGA twisted-nematic LCD that operates in amplitude modulation between the crossed polarizer and analyzer. The LCTV has 640 $\times$ 480 square pixels that are separated by a space of 40 μm $\times$ 40 μm, with each pixel electrically addressed independently. The total surface that can be scanned is therefore 2.56 cm $\times$ 1.92 cm. The sampling aperture is defined as a group of several pixels and is programmable in both size and shape, as was discussed in Section 2. The sampling aperture used in the experiments is a 20 $\times$ 20 pixels square, i.e., its size is 800 μm $\times$ 800 μm and is chosen as a trade-off between the transverse resolution and the size of the spot on the CCD. Hence the maximum number of sampling points is 32 $\times$ 24 points. The number of sampling points has a direct influence on the acquisition time, and, consequently, a first fast scan can be performed with low resolution to check the setup before the final high-precision scan is performed.

The diffraction spots are imaged by an observation lens on a CCD detector with 640 $\times$ 480 pixels of size 11 μm $\times$ 11 μm. The lenses are doublets corrected for spherical aberration, and their focal lengths range from 200 to 800 mm, depending on the dynamic range of the component to be analyzed. Shorter or longer focal lengths could obviously be used as well. A frame grabber with separate acquisition and display

Table 1. Duration of Each Elementary Operation for One Sampling Point

Operation	Duration (ms/sample)
Subaperture display on the LCTV	90
Diffraction-spot acquisition	40
Memory transfer (frame grabber to host computer)	328
Centroid estimation	31
Total	489

memories is used to control both the LCD and the CCD camera (Coreco, Model TCX with an ISA Bus).

The position of the diffraction spot is estimated by use of a classical centroid method. The spot occupies a great number of pixels, say, as many as 80×80 pixels, depending on the ratio of the aperture size to the observation distance. The centroid computation time is kept short by use of two steps: A first fast scan of the CCD image at every 20 pixels provides the position of the pixel at which the intensity is the highest. The centroid calculation is performed inside a window of 100×100 pixels that is defined around the approximate position found in step 1. The repeatability of the centroid calculation was found to be 0.1 pixel rms for 100 measurements of the position of the same spot when the observation distance d is 1 m. The angular detection threshold of the sensor can be defined as

$$\delta\theta = \frac{1}{q}\frac{p}{D},\qquad(3)$$

where p is the CCD pixel size, d is the observation distance, and q is the fractional degree of the subpixel-position estimation. The value of $q = 10$, as found experimentally, corresponds to a sensitivity of $\delta\theta = 1.4$ μrad at 1 m.

The total scanning time is approximately 3 min for 24×24 sampling points. This time is limited by the four steps involved for each sampling point, i.e., generation of the aperture on the spatial light modulator (SLM), acquisition of a video frame, transfer from the frame grabber memory to the host memory, and centroid calculation. The duration of each of these elementary steps is given in Table 1 for our setup. It can be seen from Table 1 that most of the time is consumed by unoptimized hardware transfers between the host computer and the frame grabber and between the frame grabber and the LCTV or the CCD. A further improvement in the time of acquisition of the wave front consists of generating several subapertures simultaneously on the SLM to reduce the global display time. However, scanning-time reduction is not inversely proportional to the number of subapertures generated simultaneously. Moreover, this scan technique can be applied successfully in only the case of slowly varying wave fronts to prevent any ambiguity between diffraction spots from arising. The scanning time is reduced by 35% with four sub-

apertures and by only 40% with nine subapertures. More significantly, the duration of each step could be reduced by use of optimized hardware and, especially, by use of a faster frame grabber. A ferroelectric LC SLM to replace the twisted-nematic LC would provide binary amplitude modulation with a characteristic response time better than 1 ms instead of the current 100 ms. A fast CCD or complementary metal-oxide semiconductor camera would reduce the acquisition-step duration. The centroid estimation could be performed by use of a specialized integrated circuit that is connected directly to the image sensor.

4. Wave-Front Reconstruction

A variety of wave-front reconstruction algorithms, either zonal or modal, that use the wave-front slopes are available.[1] Any wave-front reconstruction algorithm for the SHWS applies as well to the LCWS because both sensors measure the same quantities, i.e., the slopes. Zonal algorithms, either direct or iterative, estimate the wave front at the sampling points only. With modal algorithms the wave front is expressed as a linear combination of universal functions or modes. Orthogonal polynomials, for instance, form a set of universal functions. In adaptive optics Zernike polynomials are commonly used because they are suited to circular pupils and are related directly to classical optical aberrations, such as defocus, astigmatism, spherical aberrations, and coma. However, if the rectangular shape of the LCTV is considered the best basis in this case is the basis of Legendre polynomials. Theoretically, this basis includes an infinite number of polynomials, but, in practice, it has to be truncated to a given order with the consequence that high spatial frequencies of the wave front are not taken into account. We used a modal reconstruction algorithm that is based on the minimization of a least-squares criterion, as originated by Southwell.[7] We give below the basic steps of the procedure that we use; the mathematical derivations are well known and can be found in the literature.

The polynomials used are the first 48 Legendre polynomials, and the wave front is expressed as the expansion

$$W(x, y) = \sum_{n=1}^{48} a_n P_n(x, y),\qquad(4)$$

where $P_n(x, y) = P_i(x)P_j(y)$ with $n = 7j + i$. The piston term, $n = 0$, is excluded from the expansion because it cannot be sensed by a wave-front sensor that is based on the Hartmann test. The Legendre polynomials to polynomial degree 6 are given in Table 2.

After the coefficients of the decomposition on the Legendre basis are estimated it is easy to obtain the decomposition on the Zernike basis. With the piston

Table 2. First Seven Legendre Polynomials

Polynomial Degree	Legendre Polynomial
0	$P_0(x) = \dfrac{1}{\sqrt{2}}$
1	$P_1(x) = \sqrt{\dfrac{3}{2}}\, x$
2	$P_2(x) = \dfrac{1}{2}\sqrt{\dfrac{5}{2}}\,(3x^2 - 1)$
3	$P_3(x) = \dfrac{1}{2}\sqrt{\dfrac{7}{2}}\,(5x^3 - 3x)$
4	$P_4(x) = \dfrac{3}{8\sqrt{2}}\,(35x^4 - 30x^2 + 3)$
5	$P_5(x) = \dfrac{1}{8}\sqrt{\dfrac{11}{2}}\,(63x^5 - 70x^3 + 15x)$
6	$P_6(x) = \dfrac{1}{16}\sqrt{\dfrac{13}{2}}\,(231x^6 - 315x^4 + 105x^2 - 5)$

term excluded again, we use the first 28 Zernike polynomials, as given by

$$W(r, \theta) = \sum_{p=2}^{28} b_p Z_p(r, \theta). \qquad (5)$$

The unknown Zernike coefficients b_p, expressed as a function of the Legendre coefficients, are

$$b_p = \sum_{n=1}^{48} \left[\iint P_n(r, \theta) Z_p(r, \theta) r \mathrm{d}r \mathrm{d}\theta \right] a_n, \qquad (6)$$

where integration is performed over the disk contained in the rectangular LCTV pupil.

The unknown Legendre coefficients are obtained by use of the classical least-squares method that consists of minimizing the quadratic difference between the calculated and the measured slopes. The criterion is expressed as

$$E(a_1, a_2, \ldots, a_L) = \frac{1}{N} \sum_{k=1}^{N} \{ [s_{ex}(x_k, y_k) - s_{mx}(x_k, y_k)]^2$$
$$+ [s_{ey}(x_k, y_k) - s_{my}(x_k, y_k)]^2 \}, \qquad (7)$$

where L is the number of Legendre polynomials used in the reconstruction, N is the total number of sampling points, x_k and y_k are the coordinates of the center of the kth subaperture, and the subscripts e and m refer to the experimental and the estimated slopes, respectively. The choice of the number of polynomials used for reconstruction results from consideration of the range of spatial frequencies that are to be measured. High spatial frequencies filtering by the modal reconstruction algorithm leads to smoothing of the measurement noise. From knowl-

edge of the variance σ^2 of the experimental measurement noise that is assumed to be Gaussian and white and the value of the least-squares criterion found after minimization it is possible to determine the amount of reconstruction error that is due to the truncation of the polynomial expansion. The mathematical mean of the least-squares criterion is, indeed,

$$\langle E(\hat{a}_1, \hat{a}_2, \ldots, \hat{a}_L) \rangle = 2\sigma^2 - \frac{L}{N}\sigma^2$$
$$+ \text{(reconstruction error)}. \qquad (8)$$

The reconstruction error thus accounts for all information in the slope measurements that is due to modal truncation rather than to measurement noise. A large value of the criterion compared with twice the variance of the measurement noise indicates that the wave front contains high frequencies that cannot be reduced to measurement noise. A modal reconstruction algorithm with a higher number of polynomials should then be used to improve the estimation accuracy.

5. Measurement Examples

Various optical components with different characteristics were analyzed to provide evidence of the performance and characteristics of the sensor. Three examples are given in this section. We first choose a spherical divergent lens with a nominal focal length of -1 m to test the validity of the optical setup and of the reconstruction algorithm. The second example uses a thin glass plate that exhibits small phase variations to point out the high sensitivity of the sensor. The third example uses a progressive ophthalmic lens that is chosen for its high dynamic range and its absence of revolution symmetry to show that rather complicated wave fronts can be sensed with high accuracy. Note that example 3 was already given in Ref. 5. All examples are presented with the tilt coefficients removed (Zernike polynomials 2 and 3 or Legendre polynomials 1 and 7) because tilt can result from the positioning of the sample and is not part of the optical aberrations.

Figure 3(a) displays the reconstructed wave front from behind a divergent lens. The focal length used was 300 mm, and the CCD camera was positioned 20 mm behind the focal plane. The number of sampling points was set to 24×24, and the programmed subaperture on the analysis pupil was a rectangle of 800 μm $\times$ 800 μm. The reconstructed wave front is mostly a revolution paraboloid, as is expected for a lens, which means that the second-degree coefficients of the decomposition are dominant. Figures 4(a) and 4(b) show the Legendre and the Zernike expansion coefficients, respectively. The focal length of the divergent lens is easily deduced from the fourth Zernike coefficient and is found to be -0.95 m. Figure 3(b) shows the experimental slopes measured in the y direction. The surface of the slopes is mostly planar, in agreement with the shape of the wave
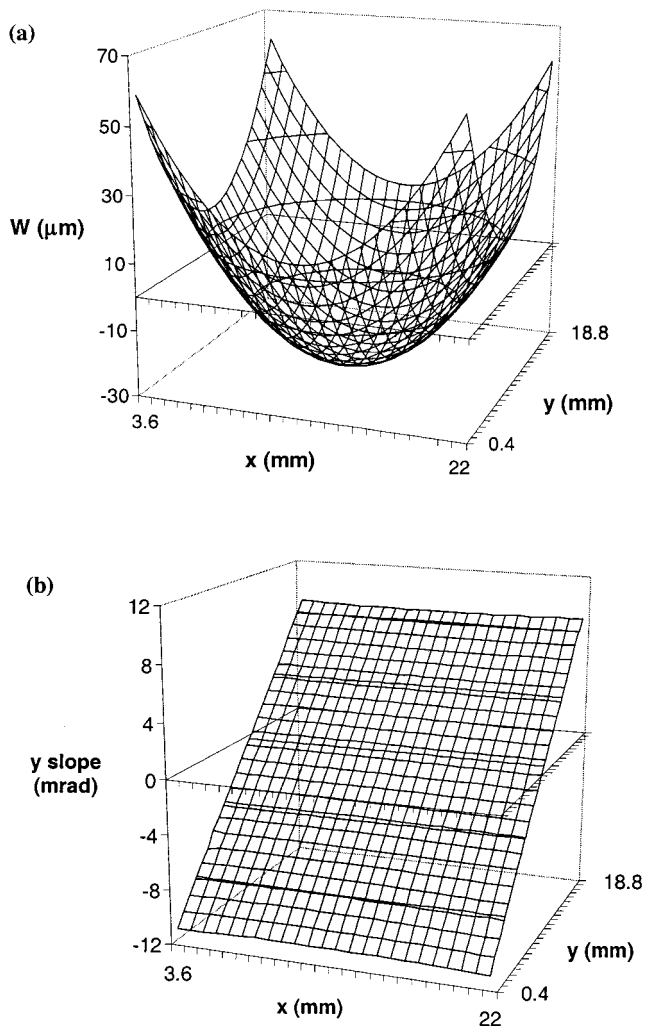
(a)

(b)

Fig. 3. Measurement of the wave front from behind a divergent lens: (a) reconstructed wave front and (b) experimental wave-front slopes along the y direction.

(a)

(b)

Fig. 4. Legendre and Zernike coefficients in the expansion of the wave front shown in Fig. 3(a).

front. The standard deviations of the reconstruction error, i.e., the square roots of the least-squares criterion defined in Eq. (8), are 30 and 25 μrad along the x and the y axes, respectively. The relative estimation error of the slopes is only 0.5%. We believe that the residual reconstruction error arises from the non-uniformity of the lens, which induces small, rapidly varying distortions on the wave front.

Figure 5(a) displays the experimental slopes in the y direction as obtained for a thin glass plate. The focal length used was 600 mm, and the camera was placed 165 mm behind the focal plane. The number of sampling points was set to 25 × 25 with a scanning aperture of 400 μm × 400 μm. Because the slope values are very small in this case, the measurement noise can be observed from the experimental data, in contrast with the divergent-lens measurements of Fig. 3(b). Figure 5(b) displays the slopes obtained with the reconstruction model. The reconstructed wave front is shown in Fig. 5(c). The standard deviations of the reconstruction error are 5 and 9 μrad
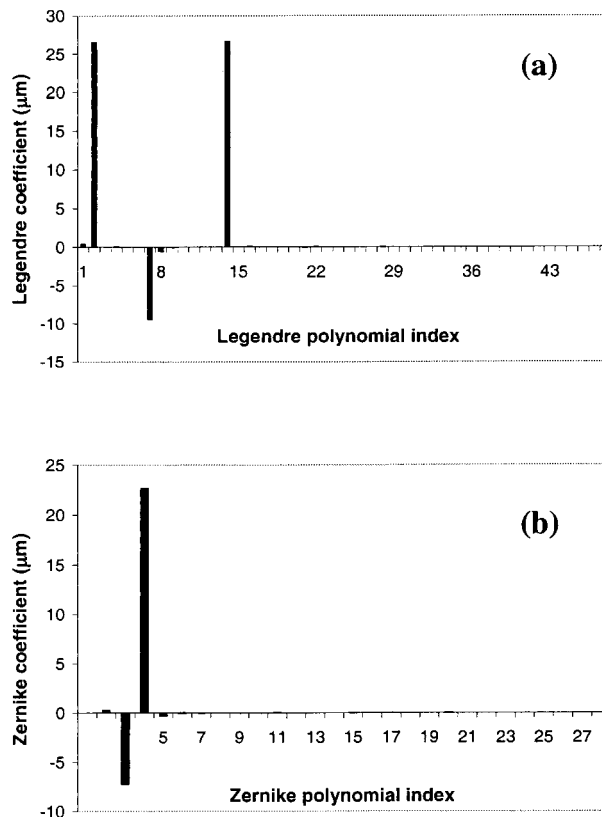
in the x and the y directions, respectively. The relative estimation error of the slopes is 0.5%, as for the previous example, although the dynamic of the wave front is much smaller.

Figures 6(a) and 6(b) display the experimental slopes for an ophthalmic progressive lens along the x and the y directions, respectively. The focal length used was 200 mm, and the observation distance was set to 170 mm. The number of sampling points is 29 × 21 with a scanning aperture of 800 μm × 800 μm. The reconstructed wave front is shown in Fig. 6(c). The curvature appears to vary along the x axis, which was the vertical axis in the experiment. These results are characteristic of a progressive lens with a vertically varying focal length—the upper part of the lens having a longer focal length than the lower part. The parameters of the ophthalmic progressive lens were not available, so an objective comparison of the measured wave front with the expected one was not possible. The standard deviations of the reconstruction error are 42 and 35 μrad in the x and the y directions, respectively, and the relative error of the slopes is again 0.5%. This relative estimation error therefore seems characteristic of the sensor.

The accuracy of the measurement of a wave front is limited, on the one hand, by the measurement noise from the experimental values of the slopes and, on the other hand, by the accuracy of the determination of the position of the diffraction spot. The detection
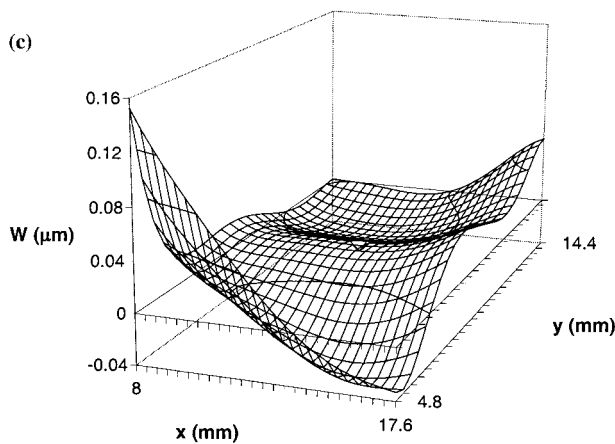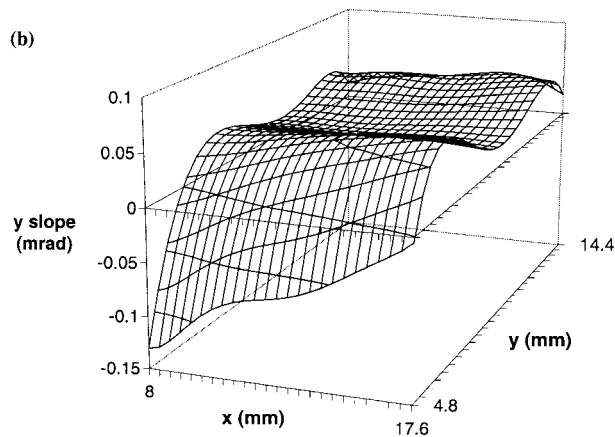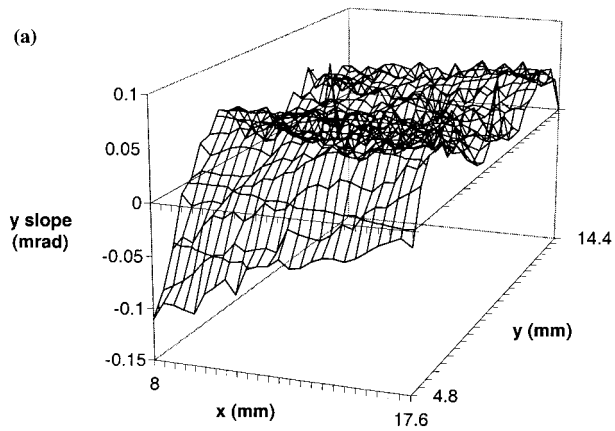
Fig. 5. Measurement of the wave front from behind a thin glass plate: (a) experimental wave-front slopes along the y direction, (b) reconstructed wave-front slopes along the y direction, (c) the reconstructed wave front.
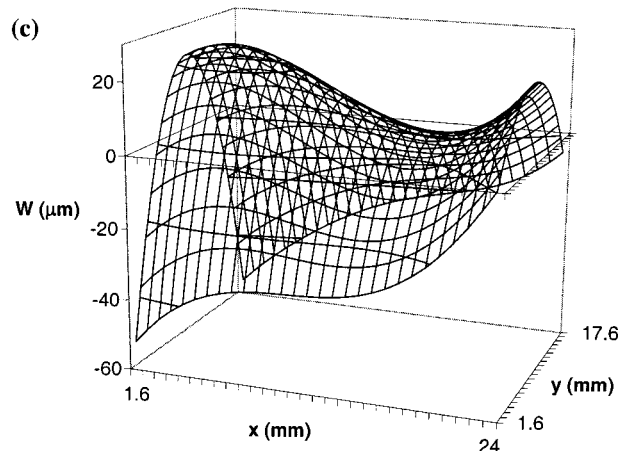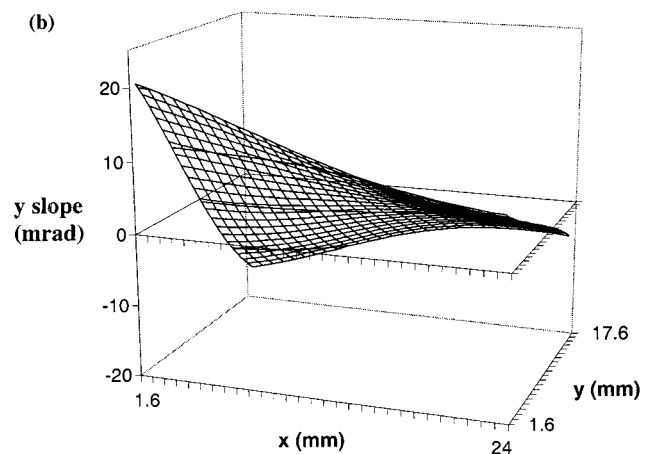

Fig. 6. Measurement of the wave front from behind a progressive ophthalmic lens: (a) experimental wave-front slopes along the x direction, (b) experimental wave-front slopes along the y direction, (c) the reconstructed wave front.

threshold of the sensor is related directly to the measurement noise. Moreover, knowledge of the measurement noise permits the estimation of the model error, as was explained in Section 4. One hundred successive measurements of the position of the same diffraction spot showed a repeatability at 0.05 pixel
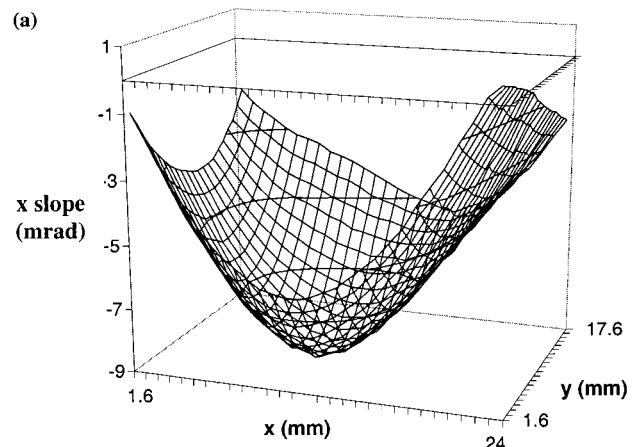
Table 3. Experimental Evaluation of the Measurement Noise as a Function of the Observation Distance

Focal Length f (cm)	Observation Distance d (cm)	Standard Deviation	
		μrad	CCD pixels
20	25	2.2	0.05
60	70	1.5	0.08
80	95	1.4	0.1

on the CCD detector when the observation distance is 25 cm, at 0.08 pixel for 70 cm, and at 0.1 pixel for 95 cm, as listed in Table 3. The measurement noise caused by mechanical vibrations, atmospheric fluctuations, and instabilities of the laser becomes greater when the observation distance increases because the displacements of the spots are amplified for the same wave-front slope. The measurement noise is less than 5 μrad for each sampling point, and the error range for the reconstructed wave front is approximately 4 nm. The expected accuracy of the wave-front reconstruction is therefore less than λ/100 over the visible-light spectrum.

Analysis of the three examples examples given above reveals that the absolute accuracy of the wave-front estimation is better for less-modulated wave fronts. However, the relative accuracy-to-dynamics ratio remains constant. For all the examples presented above the relative estimation error is 0.5%. Most of the reconstruction error arises from measurement noise, and no bias seems to be introduced by truncation of the polynomials.

6. Comparison with Other Hartmann Sensors

The resolution of a wave-front measurement is related directly to the accuracy of the local-slope measurement. Therefore an accurate measurement of the spot position on the detector is required. The exact centroid estimation would require the computation of the quantity

$$c_k = \frac{\int x' I_k(x') \mathrm{d}x'}{\int I_k(x') \mathrm{d}x'}, \quad (9)$$

where $I_k(x')$ is the intensity in the observation plane that corresponds to the kth subaperture. Instead, only a finite number of pixels are available in the observation plane, and the centroid is approximated by

$$c_k \approx \frac{\sum_q x_q' I_k(x_q')}{\sum_q I_k(x_q')}, \quad (10)$$

where x_q' is the position of the center of each acquisition pixel.

In the Shack–Hartmann sensor, the analysis pupil is an array of lenslets of short focal lengths, i.e., less than 1 cm, so the diffraction spots usually occupy a small number of pixels, say, approximately four pixels. In contrast, the diffraction spots obtained with the LCWS occupy as many as 80×80 pixels on the detector. Indeed, using a few pixels for the centroid calculation can result in a biased estimation if the spot is not perfectly centered on the group of pixels or does not present perfect revolution symmetry. Furthermore, calibration of the pixel sensitivity of the detector is a prerequisite for subpixel accuracy in the Shack–Hartmann sensor, and low-noise detection is required, as the global measurement noise for the determination of the position of one spot is proportional to σ^2/K, where σ^2 is the variance of the noise inherent to each pixel of the CCD detector and K is the number of pixels used for centroid calculation. It appears that estimating the centroid with a large number of detection pixels in the LCWS greatly reduces the sensitivity to these three error sources, i.e., biased estimation, nonuniform pixel sensitivity, and measurement noise. Hence the quality requirements on the camera can be relieved or the sensing precision can be improved. Roughly speaking, it can be said that the LCWS trades off speed of operation for resolution, as opposed to the SHWS.

A number of ray-tracing methods based on the Hartmann principle have been proposed.[8–10] In these techniques a scanning laser beam is used to sample sequentially the deviations caused by an optical system. As opposed to the SHWS and the LCWS, they are active wave-front sensors in the sense that they must include their illumination system; thus they can be used for optical testing but not for the measurement of laser beams or atmospheric turbulence. As sequential sensors, they should, in principle, share the characteristics of the LCWS, i.e., non-real-time operation and improved sensitivity. However, the mechanical scanning of the laser beam is a limiting factor for unbiased estimation and accuracy. This limitation is avoided in the LCWS because there are no moving parts.

7. Conclusions

We have discussed a new wave-front sensor that is based on the Hartmann test in which sequential scanning of the wave front is performed by the programming of small subapertures by use of a LCTV. The local slopes in two orthogonal directions are estimated by the centroid of the diffraction spot on an image sensor. The accuracy can be adjusted, depending on the dynamic range of the wave front, by changes in the focal length of the observation lens and the sampling geometry. The wave front is reconstructed from slope data on the Legendre or the Zernike polynomials basis by use of a least-squares method. Experiments with various components such as lenses, thin glass plates, and progressive lenses have proven the versatility of the device for optical testing. Compared with the SHWS the LCWS is characterized by greater sensitivity, a larger dynamic range, and higher accuracy. Moreover, the device does not specifically require a high-

quality detector. The counterpart of all these advantages is that no real-time wave-front sensing is possible because the acquisition of the wave front is sequential, which would seem to eliminate applications in adaptive optics for astronomy. However, it is a promising alternative to other wave-front sensors in the field of optical testing in which a high resolution is required and real-time operation is not essential. By slight modification of its design the LCWS can operate in the reflection instead of the transmission mode, e.g., for testing the quality of one surface of a lens only. Future improvements will probably make it possible to reduce the acquisition time.

References

1. R. K. Tyson, *Principles of Adaptive Optics* (Academic, San Diego, 1991).
2. R. V. Shack and B. C. Platt, "Production and use of a lenticular Hartmann screen," J. Opt. Soc. Am. **61,** 656 (1971); paper MG23, 1971 OSA Spring Optical Meeting.
3. J. Primot, "Three-wave lateral shearing interferometer," Appl. Opt. **32,** 6242–6249 (1993).
4. F. Roddier, "Curvature sensing and compensation: a new concept in adaptive optics," Appl. Opt. **27,** 1223–1225 (1988).
5. V. Laude, S. Olivier, C. Dirson, and J.-P. Hiugnard, "Hartmann wave-front scanner," Opt. Lett. **24,** 1796–1798 (1999).
6. V. Laude, "Twisted-nematic liquid-crystal pixelated active lens," Opt. Commun. **153,** 134–152 (1998).
7. W. H. Southwell, "Wave-front estimation from wave-front slope measurements," J. Opt. Soc. Am. **70,** 998–1006 (1980).
8. G. Häusler and G. Schneider, "Testing optics by experimental ray tracing with a lateral effect photodiode," Appl. Opt. **24,** 4160–5164 (1988).
9. C. Castellini, F. Francini, and B. Tiribilli, "Hartmann test modification for measuring ophthalmic progressive lenses," Appl. Opt. **33,** 4120–4124 (1994).
10. R. Navarro and E. Moreno-Barriuso, "Laser ray-tracing method for optical testing," Opt. Lett. **24,** 951–953 (1999).